Energy Storage Materials 35 (2021) 520–529

Contents lists available at ScienceDirect

Energy Storage Materials

journal homepage: www.elsevier.com/locate/ensm

Mechanical simulation informed rational design of a soft-and-hard double-jacketed SnO_2 flexible electrode for high performance lithium-ion battery

Xingang Liu[a], Jiamei Guo[b], Tao Liu[b], Jihai Zhang[a], Zheng Jia[b,*], Chuhong Zhang[a,*]

[a] State Key Laboratory of Polymer Materials Engineering, Polymer Research Institute of Sichuan University, Chengdu, 610065, China
[b] Key Laboratory of Soft Machines and Smart Devices of Zhejiang Province, X-Mechanics Center, Department of Engineering Mechanics, Zhejiang University, Hangzhou, 310027, China

ARTICLE INFO

Keywords:
Mechanical simulation
Graphene/SnO_2
Core-shell
Flexible electrode
Li-ion battery

ABSTRACT

Graphene-based tin dioxide (SnO_2) composite electrode is emerging as an attractive anode candidate for high-performance flexible lithium-ion batteries due to its excellent electronic conductivity, high theoretical capacity, and mechanical durability. However, the understanding of the underlying mechanism that how graphene contributes to the mechanical integrity and good electrochemical performances of flexible SnO_2 composite electrodes remains superficial. To this end, mechanical simulations aiming at directing the electrode structural design are highly desired. In this work, we reported a first-of-its-kind mechanical simulation on lithium intercalation induced stress in pristine SnO_2 anode and surface-modified SnO_2 composite anodes "wearing" soft (graphene)/hard (amorphous carbon) jacket. The simulation results quantitatively revealed that the double coatings are far more effective in reducing the charging-induced stresses and avoiding mechanical failure than pristine SnO_2 and amorphous carbon single protection. Based on this, a unique soft-and-hard double-jacketed flexible SnO_2 composite electrode with core-shelled C@SnO_2 embedded in graphene nanosheets was fabricated. In line with the mechanical simulations, the confinement of graphene encapsulation suppresses the crack formation, enhancing the mechanical integrity and the cyclic stability of the composite SnO_2 anodes. As expected, the obtained flexible anode shows high specific capacity (836 mAh•g^{-1} at 100 mAg^{-1}), excellent rate capability (506 mAh•g^{-1} at 2 Ag^{-1}) and ultra-stable cycling stability.

1. Introduction

Nowadays, numerous efforts have been devoted to developing electrochemically active metal oxides (MOs) such as SnO_2 [1–6], TiO_2 [7–9], Mn_3O_4 [10–12] and Fe_3O_4 [13–15] to meet the demand for lithium-ion batteries (LIBs) with high energy density due to their high theoretical capacities and natural abundance. As an attractive anode candidate for the next-generation high-performance LIBs, SnO_2 has a high theoretical capacity (782 mAh•g^{-1}) and low discharge potential (<1.5V) [16]. However, the commercial application of SnO_2 based anodes in LIBs is hampered by their poor cycling stability caused by huge volume variation and aggregation of tin during the Li^+ insertion/extraction, leading to pulverization of the anode and electrical detachment of active materials from current collector [17]. Strategies, such as fabricating various nanostructures [18–25], combining/coating with buffer materials [2,4,5,26,27] have been demonstrated effective in addressing the above problems associated with SnO_2. Among them, hybridizing SnO_2 with graphene has been widely studied due to the excellent intrinsic electronic conductivity, superior structural flexibility and mechanical robustness of graphene, which could not only facilitate faster electrons/ions transfer, but also improve the volume change tolerance of SnO_2 during Li^+ insertion/extraction. Other carbonaceous components have also been attempted to incorporate with SnO_2 in order to promote its rate capacities [18,28–31]. However, although it has been well acknowledged that the introduction of carbon materials could better accommodate the cyclic volume change of SnO_2, the understanding on how carbon materials improve the mechanical integrity and electrochemical performances of SnO_2 composite electrodes remains superficial. Lithiatin/delithiation induced stress is the culprit for the mechanical faliure of the cell, therefore, analysis on the stress generation in SnO_2 anodes during cycling is crucial. However, related mechanical investigation is still missing, reulsting in that modifications with carbon materials are rather intuitive than satisfactory: for example, coating an amorphous carbon layer still suffers significant capacity fading [32] because the rigid carbon coating is very likely to be ruptured along with the Li^+ insertion/extraction accompanied volume change of SnO_2; on the other hand, compounding with graphene cannot solve the problems that the unanchored SnO_2 nanoparticles (NPs) are vulnerable to

* Corresponding authors.
E-mail addresses: zheng.jia@zju.edu.cn (Z. Jia), chuchong.zhang@scu.edu.cn (C. Zhang).

https://doi.org/10.1016/j.ensm.2020.09.012
Received 2 September 2020; Received in revised form 16 September 2020; Accepted 17 September 2020
Available online 21 September 2020

either detachment from the graphene surface or agglomeration herein increased between-particle interface resistance [28,33].

In this study, mechanical simulation is utilized for the first time to model the stress development in SnO_2 composite anodes during lithiation including prisitine SnO_2, and surface-modified SnO_2 composite anodes "wearing" soft (graphene)/hard (amorphous carbon) jacket. The simulation results quantitatively revealed that graphene nanosheets and carbon double coatings can effectively reduce high mechanical stresses induced by charging, thereby better protecting the electrodes from mechanical failure. Therefore, a graphene/core-shelled C@SnO_2 paper electrode with a hierarchical sandwich nanostructure is fabricated, where SnO_2 NPs as a core encapsulated in an amorphous carbon shell are firmly embedded within the flexible graphene nanosheets. Such a design offers multiple attractive features for large-volume-change metal oxide anode materials: (1) the carbon shell can suppress the SnO_2 NPs from aggregating to large particles and inhibit the direct contact between SnO_2 nanocrystals to reduce the particle-particle interface resistance. (2) the carbon layer can act as a conducting bridge between SnO_2 NPs and graphene sheets that could provide a continuous conductive path between them, leading to a higher conductivity. (3) As indicated by the mechanical simulation, the SnO_2 NPs are wrapped in both the rigid carbon shells and flexible graphene like wearing a soft-hard double jacket, which suppresses the crack formation in SnO_2 NPs by reducing mechanical stresses experienced by the electrodes, leading to enhanced cyclic stability.

2. Experimental section

2.1. Fabrication of soft and hard double jacketed SnO_2 paper

Graphite oxide was purchased from the Sixth Element (Changzhou) Materials Technology Co., Ltd. In order to obtain Graphene oxide (GO) nanosheets dispersed in water, the solution after dialysis was sonicated for 1 h with a frequency of 40 kHz (KH-500, Kunshan, Hechuang Ultrasonic Cleaner Inc.). The flexible free-standing papers were prepared by a filtration method followed by subsequent hydrothermal reduction. SnO_2 nanoparticles were prepared by using a facile gas-liquid interfacial synthesis approach [23]. Carbon coated SnO_2 (C@SnO_2) nanocomposites were prepared by a hydrothermal approach [24,25]. Briefly, 1 g of glucose and 0.12 g of SnO_2 were dispersed in 40 mL deionized water and 20 mL of ethanol by sonication, and the resulting suspension was transferred to a Teflon-lined autoclave. Then the autoclave was sealed and placed in a drying oven at 180°C for 12 h. After cooling and centrifugation, followed by thermal treatment at 500°C for 2 h under argon atmosphere, C@SnO_2 powders were obtained.

The free-standing soft and hard double jacketed SnO_2 paper (GCSP) was prepared by simple filtration and subsequent hydrothermal reduction. First, 3 mg of C@SnO_2 was dispersed into a 3 ml GO (1 mg/ml) aqueous suspension by sonication. Then the suspension was filtrated with a filter membrane (50 mm in diameter, 200 nm in pore size) under a positive pressure to produce a paper. Finally, the flexible free-standing paper was peeled off from the filter membrane and hydrothermally reduced for 12 h at 220 °C to produce the GCSP sample. As a comparison, graphene@SnO_2 paper (GSP) was prepared by the same procedure only using pristine SnO_2 and GO aqueous suspension.

2.2. Material characterization

The crystal structures of samples were characterized by X-ray powder diffraction (XRD) analysis performed on a Rigaku Smart Lab (3) diffractometer with Cu K_α radiation, with a scan 2θ range from 10° to 80°. Morphology of the prepared powders was observed by scanning electron microscopy (SEM) (JEOL, JSM-6510), and transmission electron microscopy (TEM) (JEM-2010). The Raman spectrometer was recorded on a Lab RAM HR800 (HORIBA Jobin Yvon) confocal Raman spectrometer, with an excitation laser wavelength of 532 nm. XPS measurements were carried out with an ESCA Lab 220i-XL spectrometer using a twin-anode Al K_α (1486.6 eV) X-ray source. All spectra were calibrated to the binding energy of the C 1s peak at 284.6 eV. Thermogravimetric analysis (TGA) was carried out on a TGA-Q50 (TA Instruments Co, Ltd, America) at a heating rate of 10 °Cmin^{-1} from 30 to 750 °C in air.

2.3. Electrochemical evaluation

The electrochemical properties of GCSP, GSP, C@SnO_2 and SnO_2 samples were measured on coin cells (CR2032 coin type). For testing GCSP and GSP, the sample was cut into desired sizes and designed without using other carbon additives, polymer binders, and metal current collectors. For the C@SnO_2 and SnO_2 powders, the working electrodes were fabricated from the slurries of active materials (80 wt%), acetylene black (AB, 10 wt%), and polyvinylidene fluoride (PVDF, 10 wt%) mixed in 1-methyl-2-pyrrolidone (NMP) solvent. The slurries were then cast onto copper foil, and dried at 110°C in vacuum overnight. Li metal foil was used as the counter electrode and 1 M $LiPF_6$ in ethylene carbonate (EC): dimethyl carbonate (DMC) (1:1 in volume) solution as the electrolyte. The cells were assembled in a glove box filled with pure argon gas. Galvanostatic charge-discharge measurements were carried out between 0.01 to 3.0 V (vs. Li/Li^+) using a battery test system LAND CT2001A. Cyclic voltammetry (CV) was tested in the potential range of 0.01-3 V (vs. Li/Li^+) with a scan rate of 0.1mV/s on Biologic VMP3 electrochemical workstation. It was also employed to perform electrochemical impedance spectroscopy (EIS) measurements with an AC voltage of 5 mV over the frequency range of 10^{-2}–10^5 Hz.

2.4. Mechanical simulation

The lithiation is modelled by a nonlinear diffusion model with a diffusivity of $D = D_0[1/(1-C) - 4C]$, where D_0 is a diffusivity constant, C is the normalized Li concentration, namely, $C = 0$ represents pristine SnO_2 while $C = 1$ represents the fully lithiated phase. To describe the lithiation-induced deformation, an elastic and perfectly plastic model is adopted, with the total strain rate being a sum of three parts: $\dot{\varepsilon}_{ij} = \dot{\varepsilon}^{e}_{ij} + \dot{\varepsilon}^{p}_{ij} + \dot{\varepsilon}^{l}_{ij}$ (i=1, 2, 3 and j=1, 2, 3). Here $\dot{\varepsilon}^{e}_{ij}$ and $\dot{\varepsilon}^{p}_{ij}$ denote the elastic and plastic strain rate, respectively; $\dot{\varepsilon}^{l}_{ij}$ denotes the lithiation-induced volumetric strain rate and is related to the rate of normalized concentration $\dot{C}$ by $\dot{\varepsilon}^{l}_{ij} = \beta\delta_{ij}\dot{C}$, where β is the volume expansion coefficient and δ_{ij} the kronecher delta. The above nonlinear diffusion and elastic-perfectly plastic model is numerically implemented in the finite element package ABAQUS. In the simulations, we set up three models: (i) A freestanding SnO_2 particle, (ii) A carbon-coated SnO_2 particle, and (iii) A carbon-coated SnO_2 particle wrapped by graphene sheets. The Li concentration at the surface of the particles are set to be $C = 1$. The volume expansion coefficient β is taken to be 0.41 to yield a total volume increase of 240% caused by the formation of $Li_{4.4}Sn$. The Young's modulus E and Poisson's ratio ν of the SnO_2 particle decrease from 200 GPa and 0.3 for pristine particles to 24.7 GPa and 0.24 for the fully lithiated phases. The yield strength of the lithiated phase is taken to be 500 MPa. The carbon shell and graphene sheets are modelled with Young's modulus of 759 GPa and Poisson's ratio of 0.3. The mechanical interaction between the carbon shell and the graphene sheets is described by a hard contact behavior. NLGEOM option is turned on to account for the large nonlinear deformation during lithiation.

3. Results and discussion

Understanding the variation of mechanical stress during electrochemical cycling of an electrode material is highly demanded since stress-induced mechanical failure is essentially the culprit to the cell

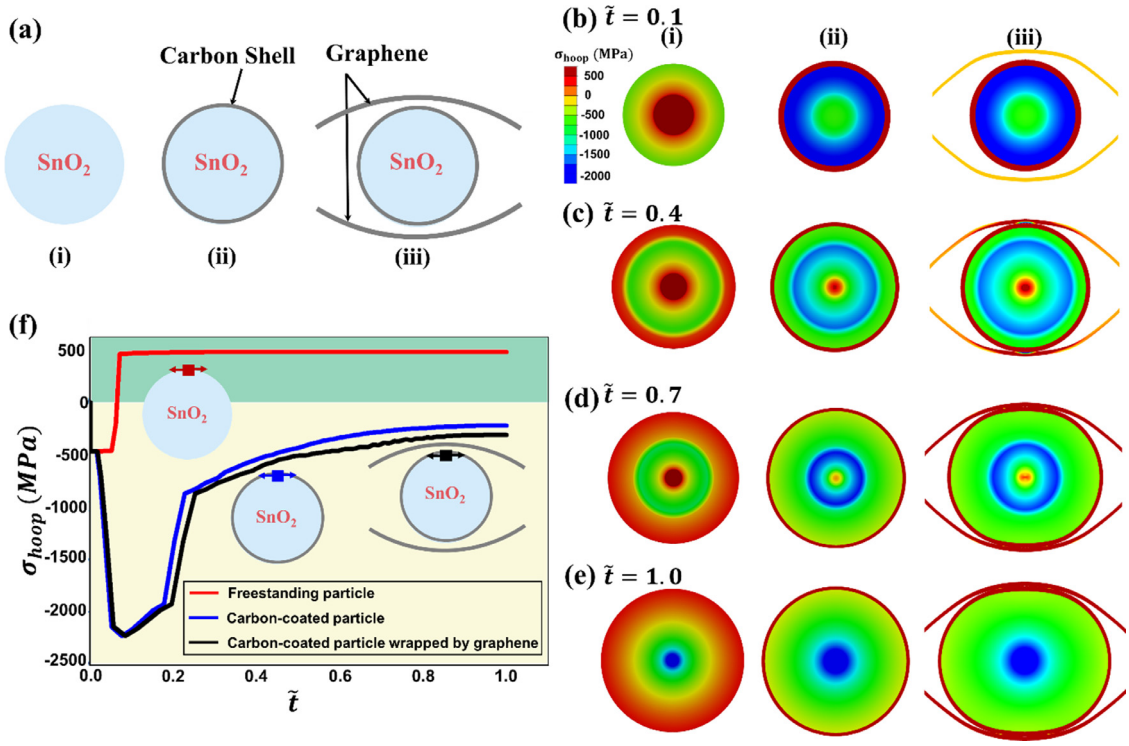

Fig. 1. Mechanical simulations of the hoop stress generation in SnO_2 particles. (a) Schematics of the simulation models. (b-e) Snapshots showing hoop stress distribution in SnO_2 particle anodes at various stages of lithiation. A SnO_2 particle, a carbon-coated SnO_2 particle, and a carbon-coated SnO_2 particle wrapped by graphene sheets are investigated. The color contour denotes the hoop stress level. (f) The evaluation of surface hoop stress during lithiation. The insets visualize the direction of the hoop stress. It is quantitatively demonstrated that the carbon coating and graphene sheets could markedly reduce the hoop stress level, thereby protecting the SnO_2 particle from catastrophic fracture.

capacity degradation. Herein, we start with mechanical modeling to investigate the stress development of nano-sized SnO_2 particles (left panel of Fig. 1a). It is critical to appreciate that the lithiation of SnO_2 particles occurs via a two-phase mechanism which features an atomically-sharp reaction front separating an inner pristine SnO_2 core and an outer shell consisting of Li_xSn (x≈4.4) and Li_2O [34]. When such a reaction front moves from the surface to the center of a particle, the insertion of lithium atoms causes a volume expansion of ~240% in the lithiated phase [34]. Notably, the inner unlithiated core constrains the hoop expansion, thereby resulting in compressive hoop stress (namely, the stress in the circumferential direction) near the reaction front. At the early stage of lithiation, the reaction front is close to the surface of the particle so that materials in the surface layer are under hoop compression (left panel in Fig. 1b, the color contour represents the magnitude of hoop stress, $\tilde{t}$ represents the normalized lithiation time, with $\tilde{t} = 0$ representing the onset of lithiation and $\tilde{t} = 1$ the time of full lithiation). As the reaction front further advances into the particle, the lithiation-induced volume expansion at the migrating reaction front gradually pushes out the outer lithiated shell, giving rise to the hoop stretch in the outer shell and, in particular, tensile hoop stress in the surface layer of the particle (left panel in Fig. 1c). Indeed, the hoop stress in the region near the particle surface remains equal to the yield stress of lithiated tin for the rest of the lithiation (left panels in Fig. 1d and e). Fig. 1f provides information about the hoop stress evolution of a representative material element in the surface layer during lithiation (the red line in Fig. 1f). In good agreement with the foregoing analysis, the state of hoop stress in the surface layer transits from initial compression to tension due to the abovementioned "push-out" effect. It is important to recognize that the high tensile hoop stress in the surface layer of the particle could trigger the crack formation and subsequent pulverization of SnO_2 particles [35].

To mitigate the high lithiation-induced stress and its ramifications in terms of fracture and pulverization, carbon coatings could be adopted to encapsulate the SnO_2 particles. Next, we examine the stress development in a carbon-coated SnO_2 particle (middle panel of Fig. 1a). As lithiation proceeds, the expansion of the SnO_2 particle is strongly restricted by the carbon shell, leading to the build-up of compressive stresses that offset the high tensile hoop stress in the particle induced by lithiation. Therefore, the hoop stress in the SnO_2 particle enclosed by carbon coatings is much less tensile relative to that in the freestanding particles (the middle panel vs. the left panel in Fig. 1b-e). Fig. 1f demonstrates that the hoop stress in the surface layer of a carbon-coated SnO_2 anode (the blue line) is much lower than that in a pristine SnO_2 particle; for example, the hoop stress at the end of charging is roughly -300 MPa and 500 MPa, in carbon-coated and pristine SnO_2 particle, respectively. The hoop compression due to the confinement of the carbon coating suppresses the crack formation and is critical for enhancing the mechanical integrity and the cyclic stability of the composite SnO_2 anodes. Nevertheless, the simulation results suggest that the carbon coating enclosing SnO_2 anodes cannot remain intact during lithiation: the volume expansion of SnO_2 anodes could break the carbon coating into pieces by engendering high tensile hoop stresses in the coating (Fig. S1a), thereby leading to mechanical degradation and capacity fading of the anodes.

It is expected that wrapping carbon-coated SnO_2 particles with graphene sheets may further enhance the mechanical integrity of the SnO_2 anodes. For simplicity, the simulation model is comprised of one carbon-coated SnO_2 particle wrapped by two arc-shaped graphene sheets (right panel of Fig. 1a). As lithiation starts, the SnO_2 particle continuously expands in volume and gradually fills the space between the particle and the graphene sheets. Before the particle and graphene sheets contact each other, the carbon-coated particle expands isotropically, with the stress profile remaining identical to that in a carbon-

coated SnO_2 particle (right vs. middle panel in Fig. 1b). As lithiation proceeds, the carbon coating and graphene come into contact and thereafter the expansion of particle in the vertical direction is restricted, leading to anisotropic expansion of the particle (right panel in Fig. 1c-d). The contact significantly reduces the large tensile hoop stresses in the carbon shell (Fig. S1b) and thus mitigate the breaking of carbon coatings caused by the expansion of the SnO_2 particle. In addition, the graphene sheets also reduce the hoop stresses in the SnO_2 particle (the black line in Fig. 1f), thereby enhancing the resistance of the anodes to mechanical degradation. Our findings have implications for the SnO_2-based electrodes for lithium-ion batteries. Mechanical confining due to carbon coating and graphene sheets could markedly enhance the fracture resistance of SnO_2 particles, which is widely believed but not quantitatively understood before. To this end, we can anticipate that a soft-and-hard double-jacketed SnO_2 flexible electrode is a promising candidate for anodes of lithium-ion batteries.

Free-standing soft-and-hard double-jacketed- graphene/core-shelled carbon@SnO_2 paper (GCSP) electrode was prepared by a facile filtration method followed by hydrothermal reduction, as shown in Fig. 2a. As prepared SnO_2 NPs were first conformally coated with a layer of glucose in deionized water and ethanol mixed solution [36]. The carbon-coated SnO_2 (C@SnO_2) NPs with core-shell structure were obtained by a hydrothermal approach and subsequently heated to 500 °C for 2 h under Ar [22]. Then the C@SnO_2 NPs were mixed with oxide graphene (GO) solution and filtrated with a filter membrane to produce a paper. Finally, the GCSP was obtained after 12 h of hydrothermal reduction at 220 °C. Graphene@SnO_2 paper (GSP) was prepared by the same procedure only using pristine SnO_2 and GO aqueous suspension.

The microstructure and morphology of SnO_2, C@SnO_2 NPs and GSP are characterized by FESEM and TEM. One can clearly see that the majority of the SnO_2 NPs aggregate together (Fig. S2a), and the primary particle sizes of them are about 6-10 nm. The NPs are well crystallized where the lattice spacing of 0.33 nm corresponds to the d-spacing of (110) diffraction planes of the rutile SnO_2 phase [37] (P_{42}/mnm, a= 4.74 Å, c=3.19 Å) (Fig. S2b). After coated with carbon, the C@SnO_2 NPs preserve their crystalline nature and are uniformly distributed in the view without obvious agglomeration, and the carbon coating shell is estimated to be about 2 nm thick (Fig. S2c, S2d). For GSP samples, it can be seen from Fig. S3e and S3f that SnO_2 NPs still exist in the form of agglomeration, which is not conducive to the improvement of electrochemical performance.

The surface morphology of GCSP shows that C@SnO_2 NPs are uniformly anchored over the plicated graphene sheets (Fig. 2b). Fig. 2c is the cross-section view of the GCSP, revealing a typical ~3 μm layered structure without any floating particles. In addition, the inset in Fig. 2c shows the digital photograph of the as-prepared GCSP, demonstrating its good flexibility. The HRTEM image (Fig. 2d) shows the details of the GCSP structure: thin carbon layers cover the SnO_2 NPs and also contact with the graphene sheets, which act as a conducting bridge between the SnO_2 NPs and the graphene sheets. Fig. 2e confirms in the composites the well-crystallized rutile SnO_2 nanoparticle with lattice fringe of 0.33 nm corresponding to the d-spacing of (110) diffraction planes. From EDS mapping images (Fig. 2f-h), one can see that there are a large amount of Sn and O elements in the hybrids, and the distribution is wide and even includes the graphene region. Fig. S3 is the TGA curve of GCSP, showing that the as-prepared GCSP lost 39.7 % of the initial weight in the temperature range of 350 to 500 °C, which can be ascribed to the decomposition of amorphous carbon and graphene. Thus, the content of SnO_2 in GCSP can be calculated as 60.3 wt. %, which is consistent with EDS result (Fig. 2i).

X-ray diffraction (XRD) measurement (Fig. 3a) indicates that all samples have the standard tetragonal SnO_2 phase (JCPDS Card No 41-1445), and no other peaks are found. It is difficult to identify graphene or carbon peaks in the GCSP diffraction pattern because of the disordered stacking characteristics of the graphene sheets and the disordered nature of the amorphous carbon. Moreover, the (110) peak of the SnO_2 overlapped with the typical (002) peak of the graphene, making it hard to distinguish. There are two typical carbon bands can be observed in Raman spectra (Fig. 3b) of GO, GSP and GCSP: G-band (1592 cm^{-1}) and D-band (1334 cm^{-1}). In general, the peak intensity ratio of D-band and G-band (I_D/I_G) is related to the degree of disorder and the average size of sp^2 domains [38, 39]. As shown, GCSP shows higher I_D/I_G value of 1.13 than GSP (1.1) and GO (1.0), which is attributed to the amorphous carbon coating and the intervention of loaded SnO_2 NPs.

XPS survey spectras of GCSP indicate the presence of the principal C1s and Sn peaks (Fig. 3c, 3d), which are consistent with XRD results. As shown in Fig. 3e, the peak of the C1s core-level spectrum of GSP can be fitted with four components: the main peak at a binding energy of 284.6 eV can be assigned to non-oxygenated C, whereas the other three oxidized C peaks, located at 286.3, 287.7 and 289.3 eV, should be assigned to carbons in C–O, carbonyl carbon (C=O), and carboxylate carbon (O–C=O), respectively [38]. For GCSP, the XPS spectra of C1s (Fig. 3f) gives binding energies at 284.7, 286.2, 287.8, and 289.2 eV. Interestingly, the ratio of non-oxygenated C to oxidized C is enhanced to 4.1 of the GCSP from 2.6 of the GSP due to the presence of the carbon coating layer on the SnO_2, which has more non-oxygenated C than graphene.

3.1. Electrochemical performance

To investigate the electrochemical performance of the GCSP, CV and galvanostatic charge/discharge measurements were tested over a voltage range of 0.01–3.0 V vs. Li^+/Li. Fig. 4a displays the CV curves for the first three cycles of the GCSP electrode. Two peaks can be observed at 0.8 V and 0.05 V on its first cathodic scan,which are characters typical of SnO_2-based anodes [36]. The peak at 0.8 V is mainly attributed to the partially reversible reduction reaction of SnO_2 to Sn ($SnO_2+4Li^++4e^-\rightarrow 2Li_2O+Sn$), and the formation of irreversible solid electrolyte interface (SEI) film [30]. While the one at 0.05 V represents the reversible alloying reaction between Li^+ and metallic Sn ($Sn+xLi^++xe^- \leftrightarrow Li_xSn$ ($0\leq x\leq 4.4$) and the intercalation of Li^+ into graphene. In the anodic scan, two corresponding peaks are well observed at ~0.53 V and ~1.25 V. The former corresponds to dealloy of Li_xSn alloy and the latter is owing to the reaction between Sn and Li_2O [30,40,41]. From the 2nd cycle onwards, the cathodic and anodic peaks reproduce very well, indicating that an excellent cyclic performance of the as-prepared GCSP. For comparison, CV curves of the pristine SnO_2 nanoparticles, C@SnO_2 and GSP electrodes are shown in Fig. S4. Their CV curves show similar electrochemical reactions during the charge/discharge process but with inferior cyclic stability.

The galvanostatic charge/discharge profiles of the GCSP at a current density of 100 mA•g^{-1} between 0.01-3.0 V (vs. Li/Li^+) are displayed in Fig. 4b. The 1st discharge curve exhibits a voltage plateau at ~0.8 V, which is in good accordance with the strong cathodic peak at ~0.8 V (vs. Li/Li^+) observed for GCSP during 1st cathodic scan in CV measurements. Furthermore, the initial discharge and charge capacities of the GCSP electrode are 1474.3 mAh•g^{-1} and 870.8 mAh•g^{-1} (based on the total mass of the hybrid material) with an initial coulomb efficiency of 59.1%, which is higher than those obtained for SnO_2 NPs (48.2%), C@SnO_2 (53.6%) and GSP (54.4%). This is attributed to the fact that carbon layer can inhibit the direct contact between SnO_2 NPs and electrolytes to reduce the amount of irreversible SEI. Up to the 50th cycle, the specific discharge capacity remains about 791 mAh•g^{-1} with a capacity retention of 91%, which is much higher than GSP (555 mAh•g^{-1}) and C@SnO_2 (600 mAh•g^{-1}) (Fig. S4b, S4c).

For the GCSP, it is striking to note that the specific discharge capacity slightly decreases during first 20 cycles and then gradually increase in the following cycles and a reversible capacity up to 836 mAh•g^{-1} could be maintained after 100 cycles, leading to an ultralow 0.04% capacity loss per cycle (Fig. 4c). The capacity fading of SnO_2 is usually associated with the pulverization of SnO_2 particles companying with the huge volumetric change upon cyclying and thus lose of contact with

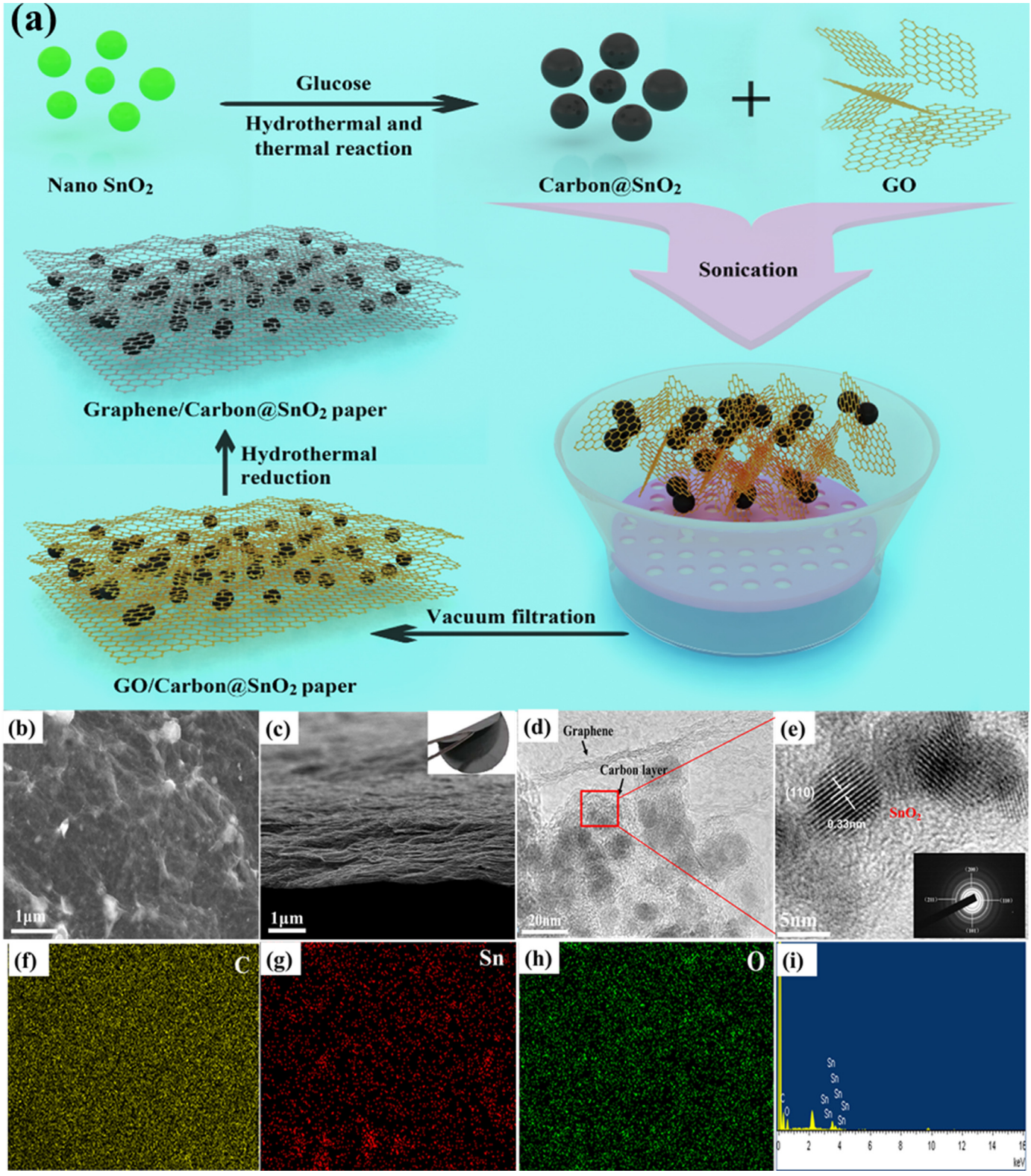

Fig. 2. (a) Schematic of the fabrication process of GCSP. FESEM (b) top and (c) cross-section view of the GCSP (inset: twisted GCSP showing good flexibility). (d) TEM and (e) HRTEM of GCSP (inset: the FFT of GCSP). EDS mapping images of (f) C, (g) Sn, and (h) O elements. (i) The analysis of EDS results of sample GCSP.

each other or with current collectors [21]. However, within a hard carbon shell, although SnO_2 particles suffer expansion in the initial a few cycles and pulverize to smaller particles, they gradually anchor onto the outer shell under the electric field force resulting in more electrochemical active sites as well as better electronic conductivity [42]. Meanwhile, the tough and elastic graphene sheets can breathe with the composite C@SnO_2 particles and prevent the carbon shell from cracking. The hard-ductile double protection is esential, considering the dramatic decay on capacity of either the C@SnO_2 NPs in the absence of the graphene structural skeleton (432 mAh•g^{-1}, 45% capacity retention at 100th cycle at a

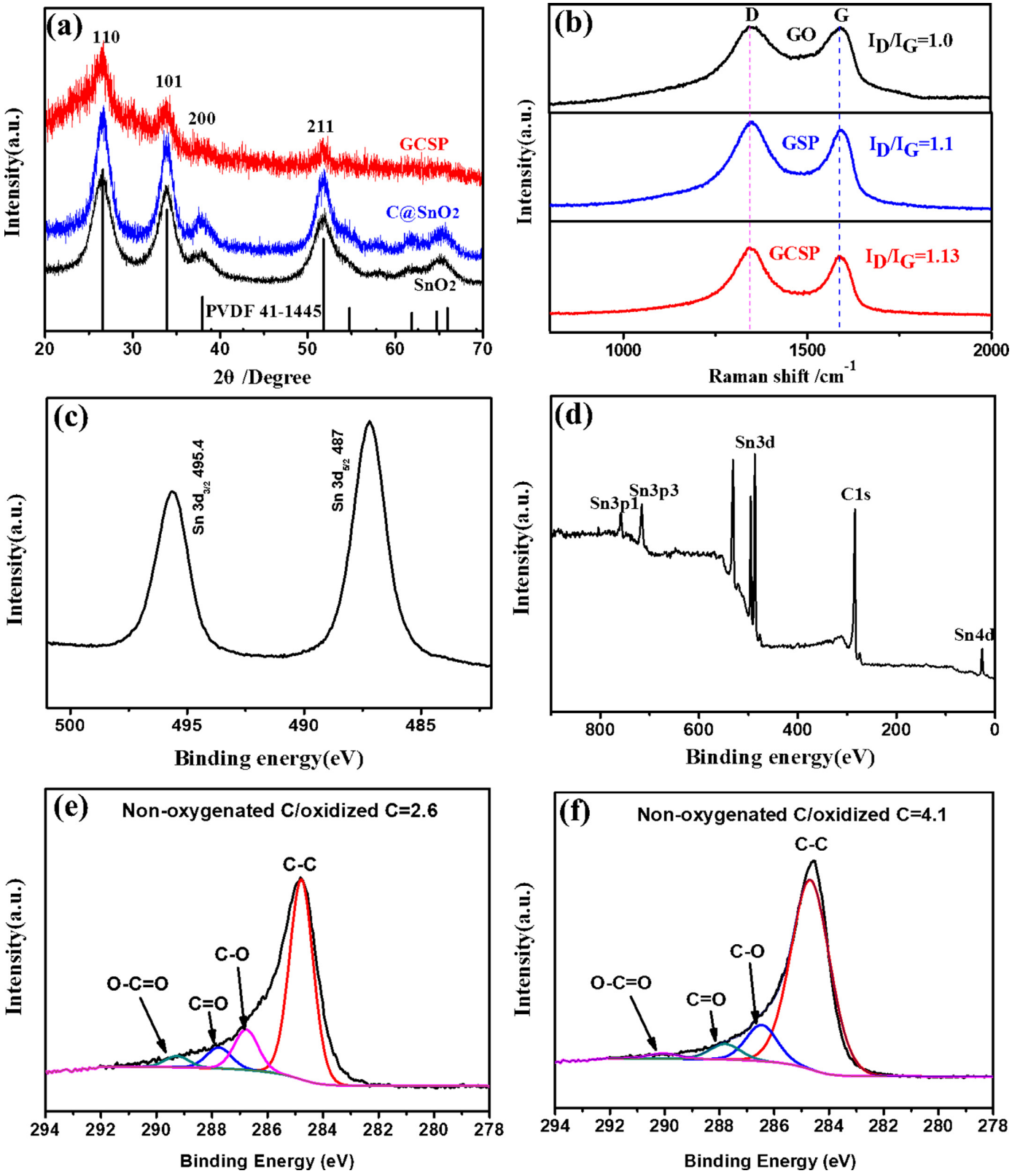

Fig. 3. (a) XRD patterns of the as-prepared SnO_2, C@SnO_2 and GCSP. (b) Raman spectra of GO, GSP and GCSP. (c) XPS Sn3d spectrum and (d) XPS survey spectra of GCSP; XPS C1s Spectra of (e) GSP and (f) GCSP.

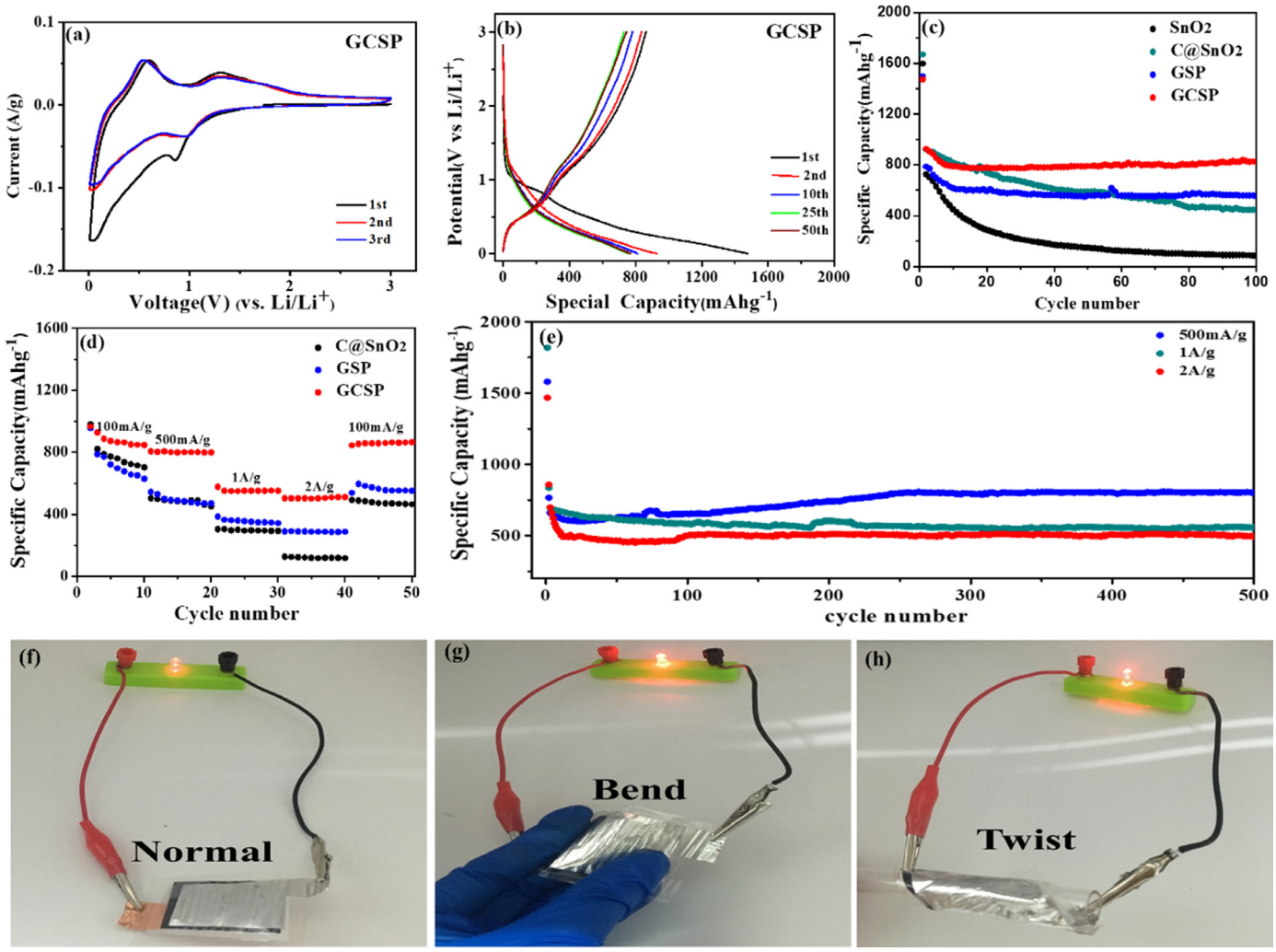

Fig. 4. (a) CV curves for the GCSP showing the first three cycles. (b) the 1st, 2nd, 10th, 25th and 50th cycle charge/discharge profiles for GCSP at a current density of 100 mA•g^{-1} in the voltage range 0.01–3.0 V. (c) Cycling performances of SnO_2, C@SnO_2, GSP and GCSP electrode at a specific current of 100 mAg^{-1} between 1 V and 3 V (vs. Li/Li^+). (d) Rate performances of C@SnO_2, GSP and GCSP electrode. (e) long-term cycling performances of GCSP at different current density between 1 V and 3 V (vs. Li/Li^+). Digital photographs of a LED lightened by the flexible battery using GCSP as the anode and lithium foil as the counter electrode under different states: (f) normal, (g) bend and (h) twist.

current density of 100 mA•g^{-1}), or the GSP where the SnO_2 NPs between the graphene nanosheets aggregate as missing the hard carbon spacers (555 mAh•g^{-1}, 69 % capacity retention at 100th cycle at a current density of 100 mA•g^{-1}). To make a further comparison, we summarized electrochemical properties of some graphene/SnO_2 flexible electrodes as shown in Table S1 [28,33,43]. It can be seen that the reversible specific capacity obtained of GCSP are comparable to those of other kinds of GNS/SnO_2 NPs flexible electrodes. It was noted that even nitrogen-doped GNS/SnO_2 NPs electrode delivered only 945 mAh g^{-1} at 50 mA g^{-1} due to the aggregation of SnO_2 NPs between graphene layers [33]. The results revealed that the dispersion of active materials can remarkably affect the electrochemical performance of GNS/SnO_2 flexible electrodes.

Moreover, the GCSP electrode exhibites enhanced rate performance, as shown in Fig. 4d. The specific capacity is maintained at values as high as 802 mAh•g^{-1} and 553 mAh•g^{-1} when the current density increases to 500 mA•g^{-1} and 1 A•g^{-1}, respectively. Even at a current density of 2 A•g^{-1}, the GCSP still deliveres a capacity of 510 mAh•g^{-1}, and the capacity can be restored to 862 mAh•g^{-1} once the current density reverses back to the intitial 100 mA•g^{-1}. The super rate capability indicates the well-maintained integrity of the flexible composite electrode. In contrast, both GSP and C@SnO_2 are far inferior at each rate, particularly with only 330 mAh•g^{-1} and 120 mAh•g^{-1} at 2 A•g^{-1}, respectively. The GCSP also demonstrates outstanding cycling stability at high rates. As shown in Fig. 4e, similar capacity boosting is also observed for electrodes cycled at higher current densities. It is obviously observed that the discharge capacity of GCSP is stabilized with a high capacity of 806 mAh•g^{-1} after 500 cycles at the current density of 500 mA•g^{-1}. Moreover, the high capacities of 558 and 506 mAh•g^{-1} are also obtained at the currents of 1 A•g^{-1} and 2 A•g^{-1} respectively, demonstrating that the results are convincing and the electrode has an excellent prolonged cycling stability.

We further demonstrated the application of GCSP in flexible batteries, where the GCSP paper was cut into desired sizes as anode and lithium metal was employed as counter electrode. As shown in Fig. 4f, a commercial LED light was illuminated successfully when contacted the pouch cell during the normal state; and even after the flexible LIB was bended (Fig. 4g) or twisted (Fig. 4h) 1000 times, the LED light was still keeping up, revealing that the GCSP electrode exhibits an attractive mechanical flexibility and electrical stability.

The above results clearly confirm that as prepared GCSP has superior cycle and rate performance, which can be ascribed to the synergistic effects of carbon layer, SnO_2, and the graphene associated with a unique core-shell and sandwiched structure. EIS measurements were

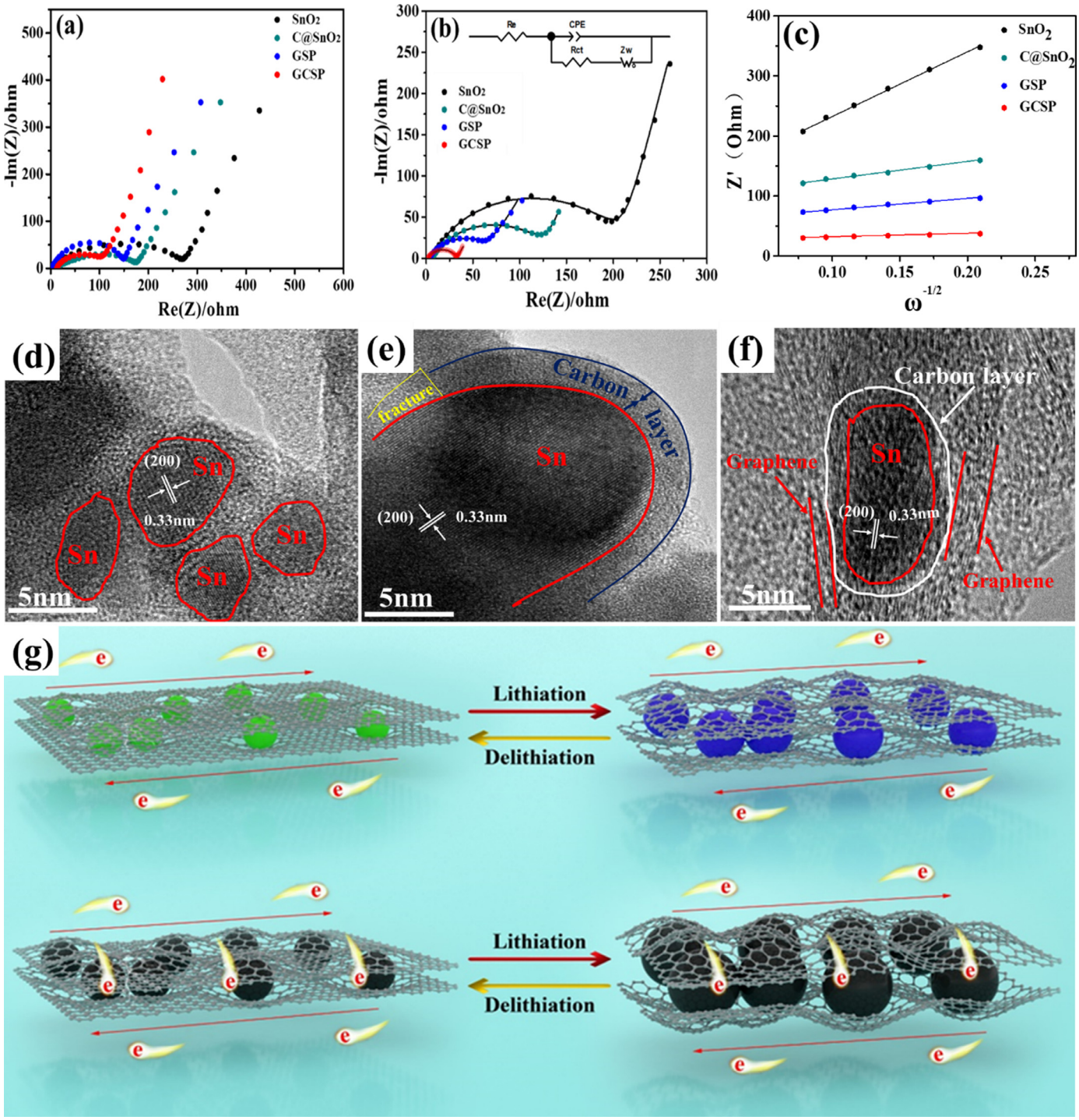

Fig. 5. Nyquist plots (a) before cycling, (b) after 100 cycles (inset: equivalent circuit used to fit the experimental data) and (c) Z_{real} *vs.* $\omega^{-1/2}$ plots of the SnO_2, $C@SnO_2$, GSP and GCSP electrodes. HRTEM inmages of (c) SnO_2, (d) $C@SnO_2$ and (e) GCSP electrodes after 100 cycles. (f) Schematic representation showing paths for electrons in the GSP and GCSP, respectively.

carried out to explore the transport kinetics of the SnO_2, $C@SnO_2$, GSP and GCSP electrodes, and the nyquist plots before and after 100 cycles are shown in Fig. 5a and b, respectively. The semicircle for GCSP in the high/medium frequency range is much smaller than that of the pristine SnO_2, $C@SnO_2$ and GSP before and after 100 cycles, suggesting a lower contact and charge-transfer resistances for the GCSP. The equivalent circuit model of the studied system is also shown in inset of Fig. 5b according to literature [39], where the R_e represents the ohmic resistance (total resistance of the electrolyte, separator and electrical contact), the charge-transfer resistance and the double layer capacitance are labeled as R_{ct} and CPE, and the Warburg impedance Z_w corresponds to the diffusion of lithium ion into the bulk electrode. The fitting parameters are listed in Table 1. The calculated total resistance (R_Ω+R_{ct}) of GCSP (32.71 Ω) is less than half of that of the other three samples. On the other hand, the electronic conductivity of GCSP (536 mS•mm^{-1}) is much higher than that of GSP (238 mS•mm^{-1}) and $C@SnO_2$ (127 mS•mm^{-1}) samples. The Li diffusion coefficient (D_{Li}) of above electrodes were determined from the Nyquist plots [44,45], and the relationships between

Table 1
Values and Li^+ diffusion coefficient of the equivalent circuit components used to fit the experimental EIS data of pristine SnO_2, C@SnO_2, GSP and GCSP samples after 100 cycles.

Sample	R_Ω(Ω)	R_{ct} (Ω)	CPE (μF)	Z_w (Ω $s^{-1/2}$)
Pristine SnO_2	5.63	209	66.63	2683
C@SnO_2	5.563	126.8	83.26	53.638
GSP	3.67	65.04	96.32	39.709
GCSP	2.05	30.66	98.36	10.386

Z_{re} and reciprocal square root of frequency ($\omega^{-1/2}$) in the low-frequency region of four samples are shown in Fig. 5c. Thus, the D_{Li} of GCSP can be calculated as 6.36×10^{-12} $cm^2 \cdot s^{-1}$, which is 2 orders of magnitude higher than pure SnO_2 (6.24×10^{-14} $cm^2 \cdot s^{-1}$). These results indicate that this unique core-shell and sandwiched structure could effectively enhance the conductivity and reduce the electrical contact resistances in the GCSP electrode.

The morphology and structure change of SnO_2 NPs, C@SnO_2 and GCSP electrode after 100 charge/discharge cycles was further investigated by HRTEM. After deep charge and discharge, the size of the nanoparticles become larger than about 10-15 nm except for SnO_2 NPs. The hoop stress generated on the surface of the SnO_2 NPs during lithiation and delithiation crush them into finer Sn particles (Fig. 5c), as predicted by the mechanical simulations. The formation of Sn is mainly due to the reduction of SnO_2, corresponding to the reaction equation $SnO_2+4Li^++4e^-\rightarrow 2Li_2O+Sn$. For C@$SnO_2$, although the carbon layer can reduce the tensile hoop stress on the particle's surface and keep it relatively intact, but there are still some cracks on the particle surface (Fig. 5d, part of yellow line). Fig. 5e shows that a single elongated C@SnO_2 nanoparticle is closely embedded between graphene layers, indicating that the excellent mechanical flexibility of the graphene layer can effectively accomodate and restrict the volume change of C@SnO_2 particle during the charge and discharge process, making its structure remains intact.

We also illustrate the transmission of electrons and the structure change process of GCSP during lithiation and delithiation. As shown in Fig. 5f, the carbon layer coated on the surface of SnO_2 can not only make it evenly dispersed, but also increase the electrical conductivity between the SnO_2 NPs and the flexible electrode in the vertical direction, thus effectively reducing the electrical contact resistances in GCSP. Moreover, as proved by mechanical simulation, the contact between graphene sheets and the carbon shell reduces the high stress level in the shell, greatly improving the electromechanical stability of the composite electrode. The above synergetic effects arising from the particular structure is responsible for the excellent electrochemical performance of the GCSP electrode.

4. Conclusions

In summary, the mechanical simulation results quantitatively demonstrated that the double coatings can effectively reduce the charging-induced stresses on the surface of pristine SnO_2 and avoid mechanical failure. The flexible soft-and-hard double-jacketed SnO_2 paper electrode with sandwich structure is rationally designed based on mechanical simulations. Benefiting from this unique hierarchical structure and the synergy protection of hard carbon shell and soft graphene sheets, the as prepared electrode possesses the features of short transportation length for electrons, excellent electronic conductivity, and dual protection to accommodate volume changes upon Li insertion/extraction, leading to an excellent cycling stability and high rate capability. This work suggests a strategy to fabricate flexible graphene–based composite paper electrodes with various large-volume-change materials which could be used to improve the electrochemical performance of flexible lithium ion batteries.

Declaration of Competing Interest

The authors declare no competing financial interest or personal relationships that could have appeared to influence the work reported in this paper.

CRediT authorship contribution statement

Xingang Liu: Methodology, Data curation, Writing - original draft. **Jiamei Guo:** Software, Visualization. **Tao Liu:** Software, Visualization. **Jihai Zhang:** Software, Visualization. **Zheng Jia:** Software, Writing - review & editing. **Chuhong Zhang:** Writing - review & editing, Project administration.

Acknowledgements

This work was financially supported by the National Key R&D Program of China (no. 2017YFE0111500), the National Natural Science Foundation of China (nos. 51933007, 51673123, and 11802269).

Supplementary materials

Supplementary material associated with this article can be found, in the online version, at doi:10.1016/j.ensm.2020.09.012.

References

[1] W. Li, Z. Chen, J. Hou, T. Xu, D. Liu, S. Leng, H. Guo, C. Chen, J. Yang, M. Wu, Appl. Surf. Sci. 515 (2020) 145902.
[2] F. Li, G. Wang, D. Zheng, X. Zhang, C.J. Abegglen, H. Qu, D. Qu, Acs Appl. Mater. Interfaces 12 (2020) 19423–19430.
[3] Y. Cheng, S. Wang, L. Zhou, L. Chang, W. Liu, D. Yin, Z. Yi, L. Wang, Small 16 (2020) 2000681.
[4] B. Jiang, Y. He, B. Li, S. Zhao, S. Wang, Y.-B. He, Z. Lin, Angew. Chem. Int. Ed. 56 (2017) 1869–1872.
[5] W. Yao, S. Wu, L. Zhan, Y. Wang, Chem. Eng. J. 361 (2019) 329–341.
[6] N. Wu, W. Du, X. Gao, L. Zhao, G. Liu, X. Liu, H. Wu, Y.B. He, Nanoscale 10 (2018) 11460–11466.
[7] G. Liu, H.H. Wu, Q. Meng, T. Zhang, D. Sun, X. Jin, D. Guo, N. Wu, X. Liu, J.K. Kim, Nanosc. Horiz. 5 (2020) 150–162.
[8] X. Zhao, H. Liu, M. Ding, Y. Feng, Ceram. Int. 45 (2019) 12476–12483.
[9] X. Zhang, B. Wang, W. Yuan, J. Wu, H. Liu, H. Wu, Y. Zhang, Electrochim. Acta 311 (2019) 141–149.
[10] Y. Yang, X. Huang, Y. Xiang, S. Chen, L. Guo, S. Leng, W. Shi, J. Alloy. Compd. 771 (2019) 335–342.
[11] M. Wang, Y. Huang, N. Zhang, K. Wang, X. Chen, X. Ding, Chem. Eng. J. 334 (2018) 2383–2391.
[12] Y. Sun, R. Jiao, X. Zuo, R. Tang, H. Su, D. Xu, D. Sun, S. Zeng, X. Zhang, Acs Appl. Mater. Interfaces 8 (2016) 35163–35171.
[13] Y. Wang, L. Chen, H. Liu, Z. Xiong, L. Zhao, S. Liu, C. Huang, Y. Zhao, Chem. Eng. J. 356 (2019) 746–755.
[14] Z. Liu, X.Y. Yu, U. Paik, Adv. Energy Mater. 6 (2016) 1502318.
[15] S.H. Lee, S.H. Yu, J.E. Lee, A. Jin, D.J. Lee, N. Lee, H. Jo, K. Shin, T.Y. Ahn, Y.W. Kim, H. Choe, Y.E. Sung, T. Hyeon, Nano Lett. 13 (2013) 4249–4256.
[16] Z.S. Wu, G. Zhou, L.C. Yin, W. Ren, F. Li, H.M. Cheng, Nano Energy 1 (2012) 107–131.
[17] W.J. Zhang, J. Power Sources 196 (2011) 13–24.
[18] P. Wu, N. Du, H. Zhang, C. Zhai, D. Yang, Acs Appl. Mater. Interfaces 3 (2011) 1946–1952.
[19] L. Ji, Z. Tan, T. Kuykendall, E.J. An, Y. Fu, V. Battaglia, Y. Zhang, Energ. Environ. Sci. 4 (2011) 3611–3616.
[20] S. Ding, D. Luan, F.Y.C. Boey, J.S. Chen, X.W. Lou, Chem. Commun. 47 (2011) 7155–7157.
[21] J.Y. Huang, L. Zhong, C.M. Wang, J.P. Sullivan, W. Xu, L.Q. Zhang, S.X. Mao, N.S. Hudak, X.H. Liu, A. Subramanian, H. Fan, L. Qi, A. Kushima, J. Li, Science 330 (2010) 1515–1520.
[22] X. Sun, J. Liu, Y. Li, Chem. Mater. 18 (2006) 3486–3494.
[23] X.W. Lou, Y. Wang, C. Yuan, J.Y. Lee, L.A. Archer, Adv. Mater. 18 (2006) 2325–2329.
[24] Y. Wang, J.Y. Lee, H.C. Zeng, Chem. Mater. 17 (2005) 3899–3903.
[25] S.J. Han, B.C. Jang, T. Kim, S.M. Oh, T. Hyeon, Adv. Funct. Mater. 15 (2005) 1845–1850.
[26] L.Y. Li, T. Chen, F.B. Huang, P. Liu, Q.R. Yao, F. Wang, J.Q. Deng, Front. Mater. Sci. 14 (2020) 133–144.
[27] W. Zhou, C. Cheng, J. Liu, Y.Y. Tay, J. Jiang, X. Jia, J. Zhang, H. Gong, H.H. Hng, T. Yu, H.J. Fan, Adv. Funct. Mater. 21 (2011) 2439–2445.
[28] J. Liang, Y. Zhao, L. Guo, L. Li, Acs Appl. Mater. Interfaces 4 (2012) 5742–5748.
[29] T. Chen, L. Pan, X. Liu, K. Yu, Z. Sun, Rsc Adv. 2 (2012) 11719–11724.
[30] J. Lin, Z. Peng, C. Xiang, G. Ruan, Z. Yan, D. Natelson, J.M. Tour, Acs Nano 7 (2013) 6001–6006.

[31] C. Zhang, X. Peng, Z. Guo, C. Cai, Z. Chen, D. Wexler, S. Li, H. Liu, Carbon 50 (2012) 1897–1903.
[32] G. Derrien, J. Hassoun, S. Panero, B. Scrosati, Adv. Mater. 19 (2007) 2336–2340.
[33] X. Wang, X. Cao, L. Bourgeois, H. Guan, S. Chen, Y. Zhong, D.-M. Tang, H. Li, T. Zhai, L. Li, Y. Bando, D. Golberg, Adv. Funct. Mater. 22 (2012) 2682–2690.
[34] L.Q. Zhang, X.H. Liu, Y. Liu, S. Huang, T. Zhu, L. Gui, S.X. Mao, Z.Z. Ye, C.M. Wang, J.P. Sullivan, J.Y. Huang, Acs Nano 5 (2011) 4800–4809.
[35] X.H. Liu, L. Zhong, S. Huang, S.X. Mao, T. Zhu, J.Y. Huang, Acs Nano 6 (2012) 1522–1531.
[36] P. Lian, X. Zhu, S. Liang, Z. Li, W. Yang, H. Wang, Electrochim. Acta 56 (2011) 4532–4539.
[37] X. Li, X. Meng, J. Liu, D. Geng, Y. Zhang, M.N. Banis, Y. Li, J. Yang, R. Li, X. Sun, M. Cai, M.W. Verbrugge, Adv. Funct. Mater. 22 (2012) 1647–1654.
[38] L. Yu, C. Falco, J. Weber, R.J. White, J.Y. Howe, M.-M. Titirici, Langmuir 28 (2012) 12373–12383.
[39] M. Zhang, D. Lei, Z. Du, X. Yin, L. Chen, Q. Li, Y. Wang, T. Wang, J. Mater. Chem. 21 (2011) 1673–1676.
[40] H.G. Wang, Q. Wu, Y. Wang, X. Wang, L. Wu, S. Song, H. Zhang, Adv. Energy Mater. 9 (2019) 1802993 1-1802993.10.
[41] L.P. Wang, Y. Leconte, Z. Feng, C. Wei, Y. Zhao, Q. Ma, W. Xu, S. Bourrioux, P. Azais, M. Srinivasan, Z.J. Xu, Adv. Mater. 29 (2017) 1603286.
[42] S. Liang, X. Zhu, P. Lian, W. Yang, H. Wang, J. Solid State Chem. 184 (2011) 1400–1404.
[43] T. Gao, K. Huang, X. Qi, H. Li, L. Yang, J. Zhong, Ceram. Int. 40 (2014) 6891–6897.
[44] Y. Cheng, J. Huang, J. Li, Z. Xu, L. Cao, H. Ouyang, J. Yan, H. Qi, J. Alloy. Compd. 658 (2016) 234–240.
[45] Q. Xi, J. Huang, J. Li, Y. Jie, T. Wang, L. Cao, C. Wang, P. Guo, J. Alloy. Compd. 786 (2019) 1013–1020.